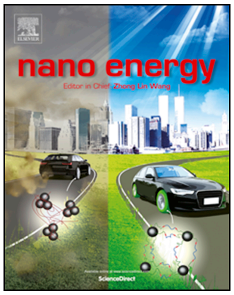

Construction of ultrafine ZnSe nanoparticles on/in amorphous carbon hollow nanospheres with high-power-density sodium storage

Shiyao Lu, Tianxiang Zhu, Hu Wu, Yuankun Wang, Jiao Li, Amr Abdelkader, Kai Xi, Wei Wang, Yanguang Li, Shujiang Ding, Guoxin Gao, R. Vasant Kumar

PII: S2211-2855(19)30196-X

DOI: https://doi.org/10.1016/j.nanoen.2019.03.008

Reference: NANOEN 3527

To appear in: *Nano Energy*

Received Date: 10 November 2018

Revised Date: 4 February 2019

Accepted Date: 2 March 2019

Please cite this article as: S. Lu, T. Zhu, H. Wu, Y. Wang, J. Li, A. Abdelkader, K. Xi, W. Wang, Y. Li, S. Ding, G. Gao, R.V. Kumar, Construction of ultrafine ZnSe nanoparticles on/in amorphous carbon hollow nanospheres with high-power-density sodium storage, *Nano Energy* (2019), doi: https://doi.org/10.1016/j.nanoen.2019.03.008.

Graphical Abstract

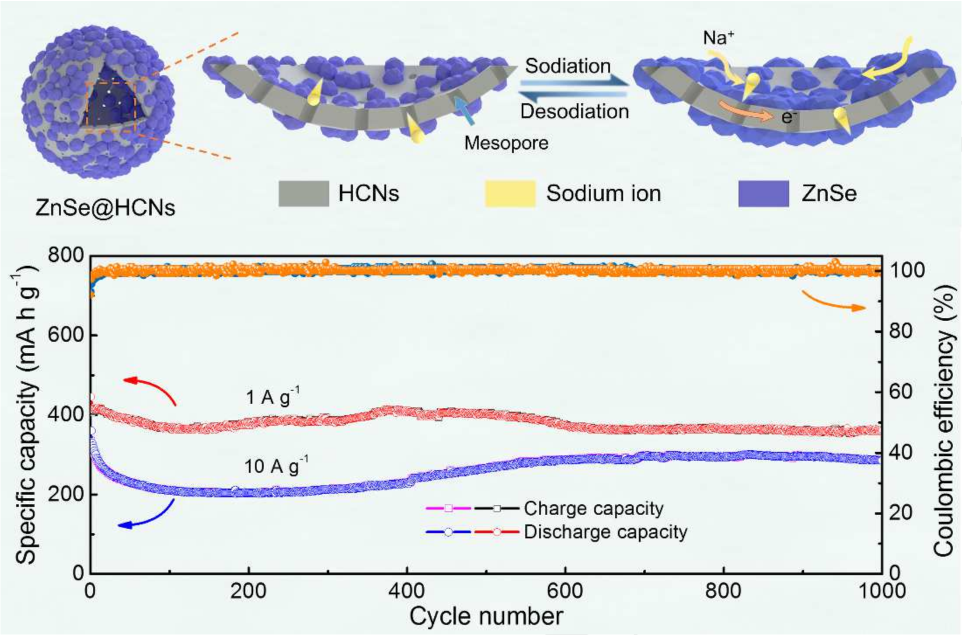

A hierarchical hybrid nanocomposite of ultrafine ZnSe nanoparticles growing on/in amorphous hollow carbon nanospheres (ZnSe@HCNs) has been prepared via simple solution reflux and post-calcination in Ar/H_2. The ZnSe nanoparticles grow on both sides of HCNs, thus preventing severe aggregation and stabilizing structures of electrodes upon cycling. When used as a promising anode for SIBs, the hybrid composites could manifest excellent electrochemical performance with high reversible capacity, long-term cyclic stability and excellent rate capability.

Construction of ultrafine ZnSe nanoparticles on/in amorphous carbon hollow nanospheres with high-power-density sodium storage

Shiyao Lu[a], Tianxiang Zhu[a], Hu Wu[a], Yuankun Wang[a], Jiao Li[a], Amr Abdelkader[b,c], Kai Xi[b, *], Wei Wang[b], Yanguang Li[d], Shujiang Ding[a], Guoxin Gao[a, *], and R. Vasant Kumar[b]

[a] Department of Applied Chemistry, School of Science, Xi'an Key Laboratory of Sustainable Energy Materials Chemistry, MOE Key Laboratory for Nonequilibrium Synthesis and Modulation of Condensed Matter, Xi'an Jiaotong University, Xi'an 710049, People's Republic of China

[b] Department of Materials Science and Metallurgy, University of Cambridge, Cambridge CB3 0FS, United Kingdom

[c] Department of Design and Engineering, Faculty of Science & Technology, Bournemouth University, Poole, Dorset, BH12 5BB, United Kingdom

[d] Institute of Functional Nano&Soft Materials (FUNSOM), Jiangsu Key Laboratory for Carbon-Based Functional Materials and Devices, Soochow University, Suzhou 215123, China

* Corresponding author. E-mail addresses: gaoguoxin@mail.xjtu.edu.cn (G. X. Gao),
kx210@cam.ac.uk (K. Xi)

Abstract

Sodium-ion batteries (SIBs) are considered as a promising candidate to lithium-ion batteries (LIBs) owing to the inexpensive and abundant sodium reserves. However, the application of anode materials for SIBs still confront rapid capacity fading and undesirable rate capability. Here we simultaneously grow ultrafine ZnSe nanoparticles on the inner walls and the outer surface of hollow carbon nanospheres (ZnSe@HCNs), giving a unique hierarchical hybrid nanostructure that can sustain a capacity of 361.9 mAh g^{-1} at 1 A g^{-1} over 1000 cycles and 266.5 mAh g^{-1} at 20 A g^{-1}. Our investigations indicate that the sodium storage mechanism of ZnSe@HCNs electrodes is a mixture of alloying and conversion reactions, where ZnSe converts to Na_2Se and $NaZn_{13}$ through a series of intermediate compounds. Also, a full cell is constructed from our designed ZnSe@HCNs anode and $Na_3V_2(PO_4)_3$ cathode. It delivers a reversible discharge capacity of about 313.1 mAh g^{-1} after 100 cycles at 0.5 A g^{-1} with high Columbic efficiency over 98.2%. The outstanding sodium storage of as-prepared ZnSe@HCNs is attributed to the confinement of ZnSe structural changes both inside/outside of hollow nanospheres during the sodiation/desodiation processes. Our work offers a promising design to enable high-power-density electrodes for the various battery systems.

Keywords: ZnSe; Hollow carbon spheres; Sodium-ion battery; Full cell; Anode.

1. Introduction:

Rechargeable lithium-ion batteries are now one of the most widely used power sources for portable electronic devices, such as mobile phone, laptop and digital camera.[1-3] LIBs are usually composed of two electrodes: a graphite anode and a layered transition metal oxide (mostly cobalt-based) cathode.[4] Both cobalt and lithium have limited supplies and their prices are expected to increase which raise concerns about the future market demands for LIBs.[5] Therefore, sodium-ion batteries have rapidly evolved as an alternative to LIBs. While SIBs share the same architecture and working principles with LIBs, they use low cost and more abundant raw materials which make SIBs strong candidates for the next-generation large-scale electrical energy storage.[6] However, sodium ions possess larger molar mass and ionic radius than lithium ions, which limits the theoretical energy density and the rate performance of SIBs as compared with LIBs.[7-9] Therefore, it is crucial to explore suitable Na-host electrode materials to accommodate the reversible insertion/deinsertion of Na^+ ions upon the continuous discharge/charge cycling, finally aiming to obtain excellent electrochemical performance.

Up to now, many anode materials have also been investigated, including metallic sulfides,[10-12] phosphides,[13] and alloys.[14] Among them, transition metal selenides (TMSs) have received considerable attention due to their high initial Coulombic efficiency, excellent electric conductivity, and good cycling stability.[15-19] However, as illustrated in **Figure 1**, bulk metal selenides still suffer from dramatic volume variation and particles agglomeration during the repeated charge-discharge process, thus causing severe polarization and rapid capacity fading problems.[20-22] One popular strategy to decline the performance decrease is to design suitable Na-host electrodes that can accommodate the reversible insertion/desertion of Na^+ ions upon the repeated cycling.[23, 24] The carbon matrix is commonly adopted to alleviate the severe volume expansion of electrode materials. Nevertheless, the bulk composites still face cracking during extended cycling.[25] Other researchers aim to construct hollow carbon materials to support nanosized TMSs, which present enhanced cycling performance.[26, 27] But the unnecessary inner void space significantly decreases the tap density and power density. Thus, designing a porous hollow carbon material to load TMSs both inside/outside could significantly enhance the cycling performance and power density.

Zinc selenide (ZnSe) has a high theoretical capacity based on the alloying and conversion reactions.[28, 29] ZnSe is also widely used in various laser devices,[30] semiconductors,[31] and solar cells,[32] which may help the commercial use of it for energy storage. Several researchers have investigated the application of ZnSe-based electrodes for LIBs. For example, Wu and co-workers reported that ZnSe composite with hollow carbon could deliver a high reversible discharge capacity of 1134 mAh g^{-1} after cycled for 500 cycles at 0.6 A g^{-1}.[33] Qian et al explained the reason for the extra rising capacity by the generation and the activation of Se during the electrochemical process.[34] More recently, Mai and his group used ZnSe microspheres (ZnSe MSs)-CNT composite as an anode for SIBs, and the results indicated the possibility of delivering capacity of 387 mAh g^{-1} for 180 cycles.[35] The ZnSe composite still showed aggregation problems to some extent, which is expected to reduce the cycle-life performance of electrodes. Therefore, it is essential to engineering a more robust electrode that can accommodate the structural changes in the ZnSe during the insertion/desertion of Na^+ ions.

In this research, we successfully developed a novel hierarchical hybrid nanocomposite of ultrafine ZnSe nanoparticles directly growing on the outer surface and in the inner cavity of amorphous hollow carbon nanospheres (ZnSe@HCNs) via a facile hydrothermal process using sulfonated polystyrene (SPS) hollow nanospheres as templates and high-temperature calcination. The ZnSe nanoparticles grow on both sides of HCNs walls for the first time (**Table S1**, see Supporting Information), thus successfully preventing the severe aggregation and ensuring the structural integrity of ZnSe@HCNs electrodes during cycling. Compared to the aggregated ZnSe microspheres (ZnSe MSs), numerous ultrafine ZnSe nanoparticles firmly anchored onto the conductive HCNs provided a more accessible surface to carry out high ratio surface and near-surface redox reactions. Therefore, the ZnSe@HCNs electrode demonstrated long-term cycle stability and high-rate performance. After 1000 cycles at 1.0 A g^{-1}, the ZnSe@HCNs anodes can deliver a stable reversible discharge capacity of 361.9 mAh g^{-1} with the capacity retention of 87.0% and Coulombic efficiency above 99.9%. Even when cycled at a high current density of 20.0 A g^{-1}, a discharge capacity of 266.5 mAh g^{-1} could still be maintained, revealing excellent high-rate capability. Moreover, the subsequently assembled $Na_3V_2(PO_4)_3$ (NVP)//ZnSe@HCNs full-cells also give an adequate capacity of 313.1 mAh g^{-1} after 100 cycles at 0.5 A g^{-1}. The well-designed ZnSe@HCNs hybrid anode shows excellent promise in sodium-ion storage.

2. Experimental section:

2.1. Synthesis of hollow sulfonated polystyrene (SPS) nanospheres

All reagents were analytical grade and used without further purification. The hollow polystyrene (PS) nanospheres were prepared by drying the emulsion (EPRUI Nanoparticles & Microspheres Co. Ltd). 35 mL of concentrated sulfuric acid and 2 g of PS were mixed at 40 ^{o}C for 12 h in an oil bath with vigorous stirring. Then the precipitate was collected by centrifugation and washed with ice water and ethanol. As a result, primrose yellow hollow SPS templates were obtained. After the sulfonation treatment, the SPS templates are capable of absorbing metal ions and inducing the growth of nanostructured metal selenides.

2.2. Synthesis of ZnSe@HCNs

In a typical fabrication of ZnSe@HCNs, 50 mg of SPS was firstly dispersed in 20 mL of deionised water by ultrasonication for 30 min to form a homogeneous suspension, followed by the addition of 1.0 mmol of $Zn(NO_3)_2 \cdot 6H_2O$, 1.0 mmol of $Na_2SeO_4 \cdot 10H_2O$ and 0.5 g of citric acid. After stirring for 30 min, 15 mL of hydrazine hydrate ($N_2H_4 \cdot H_2O$) solution (80 %) and 5 mL of ethylenediamine were added dropwise into the mixture. The above suspension was continuously stirred for another 30 min and then transferred into a Teflon-lined stainless-steel autoclave (50 mL). The autoclave was sealed tightly and heated at 180 °C for 24 h. After cooling to room temperature naturally, the pale brown precursor was centrifuged and washed thoroughly with deionized water and absolute ethanol for three times, respectively. The as-prepared precursor was subsequently dried in a vacuum oven at 60 °C overnight. Finally, the precursor was sintered at 700 °C for 2h in Ar/H_2 (90:10, v/v) mixing flow to form the final product (ZnSe@HCNs). For comparison, the aggregated ZnSe microspheres (MSs) were also prepared via a similar procedure only without adding SPS templates.

2.3. Material Characterization

The morphology and structure of the products were characterized by Field-emission scanning electron microscope (FESEM; JEOL JSM-6700F) and Transmission electron microscope (TEM;

JEOL JEM-2100F and JEM-F200) with selected-area electron diffraction pattern (SAED) function. Energy dispersive X-ray spectroscopy (EDX) measurements were performed on a FEI Quanta 250 FEG SEM. The powder X-ray diffraction (XRD; Bruker AXS D8 Advance) was used to detect the crystallographic information of samples. Thermogravimetric analysis (Perkin-Elmer TGA 7) was carried out under a flow of air with a rate of 10 °C min^{-1} from room temperature to 700 °C. Raman spectroscopy was performed on a Raman spectrometer with a backscattering geometry (λ = 633 nm; Horiba JobinYvon, HR 800). The specific surface area and pore size of as-prepared ZnSe@HCNs and aggregated solid ZnSe MSs were obtained by N_2 sorption measurement and BET analyser (ASAP 2020 PLUS HD88). The chemical compositions and valence states of resultant samples were investigated by X-ray photoelectron spectroscopy (XPS) measurements on ESCA Lab 250 (USA) at monochromatic Al K sources.

2.4. Electrochemical measurements

The electrochemical tests were conducted by assembling coin-type half-cells (CR2032) in an argon-filled glove box (Dellix, $[O_2]$<1 ppm, $[H_2O]$<1 ppm) with metallic sodium discs as the counter and reference electrodes. The working electrodes were prepared by mixing 80 wt% of electroactive materials (e.g. ZnSe@HCNs), 10 wt% of carbon black (Super-P-Li) and 10 wt% of polymer binder (sodium carboxymethylcellulose; NaCMC) in deionized water. The obtained homogeneous slurry was evenly pasted onto Cu foil (current collector) and dried in a vacuum oven at 100 °C overnight. The loading mass of active materials on the current collector is about 1.5 mg cm^{-2}. The electrolyte in the cells was 1.0 M sodium trifluoromethanesulfonate ($NaCF_3SO_3$) dissolved in diethylene glycol dimethyl ether (DEGDME). Glass fibre filter paper was used as the separator. Cyclic voltammetry (CV) and electrochemical impedance spectroscopy (EIS) were carried out on CHI660D electrochemical workstation. Galvanostatic discharge/charge cycles were performed on a NEWARE battery tester in a voltage range of 0.1 to 3.0 V in a thermotank at the temperature of 28 °C.

For comparison, the carbonate-based electrolytes including 1.0 M $NaClO_4$ in propylene carbonate (PC) with 5 wt% fluoroethylene carbonate (FEC) and 1.0 M $NaPF_6$ in ethylene carbonate/dimethyle carbonate (EC/DEC; v/v=1:1) were also used to investigate the cycle stability of as-prepared ZnSe@HCNs through assembling coin-type half-cells.

To further estimate the electrochemical performance of as-prepared ZnSe@HCNs, flower-like $Na_3V_2(PO_4)_3$ (NVP) was used as cathodic materials to assemble NVP//ZnSe@HCNs full cells. Before the preparation of full cells, ZnSe@HCNs anodes were electrochemically activated for three cycles. Then NVP cathodes and activated ZnSe@HCNs anodes were paired in a weight ratio of 8:1 with 1.0 M $NaCF_3SO_3$ in DEGDME as the electrolyte.

3. Result and discussion:

The fabrication process of the hierarchical hybrid ZnSe@HCNs composite is illustrated schematically in **Figure 2A**. Briefly, the hollow polystyrene (PS) nanospheres were firstly sulfonated by concentrated sulfuric acid to produce oxygen functional groups ($-SO_3H$). The oxygenated groups could link both Zn^{2+} and SeO_4^{2-} ions to the carbon spheres which act as the support backbone to control the nucleation and the growth of ZnSe precursor. During the nucleation process, hydrazine hydrate was added to satisfy a reduction atmosphere and to avoid the back oxidation of ZnSe precursors.[36] Ethylenediamine was also added in the hydrothermal processes to create mesoporous channels within the shell of the nanospheres through the pyrolysis and the formation of gases such as NH_3 and CO_2. These mesoporous channels promoted the diffusion and the permeation of Zn^{2+} and SeO_4^{2-} ions into the internal cavity of hollow PS spheres, which led to the formation of ZnSe nanoparticles inside the spheres cavity.[27] Next, the precursor was calcined at 700 °C for two h with a ramping speed of 2 $^{o}C\ min^{-1}$ in Ar/H_2 mixture atmosphere (90:10, v/v). The calcination process converted the ZnSe precursor to crystalline nanoparticles and at the same time carbonised the PS templates into mesoporous HCNs.

Field Emission Scanning Electron Microscope (FESEM) and Transmission electron microscopy (TEM) were used to study the morphology of PS nanospheres before and after sulfonation. As shown in **Figure 2B** and **C**, the sulfonated PS nanospheres still maintained the integrity of the spheres without noticeable distortion. The size of the nanospheres was also similar to the pure PS nanosphere (**Figure S1**, see Supporting Information), i.e. 400 nm average diameter and 50 nm shell thickness, indicating that the sulfonating process does not affect the structure of the nanospheres. After the hydrothermal reaction and the post-calcination treatment in Ar/H_2, numerous fine ZnSe particles are uniformly anchored on the surface of the HCNs with a diameter ranging from 10 to 80 nm as shown in **Fig. 2D** and **E**. Interestingly, the TEM images (**Figure 2F** and **G**) and the high-angle annular dark field scanning transmission electron microscopy (HAADF-STEM) image (**Figure 2J**) of the ZnSe@HCNs show that the ZnSe nanoparticles are also embedded within the internal cavity of the HCNs. There are no obvious aggregation or clusters of ZnSe nanoparticles can be observed by the TEM or FESEM images, confirming the uniform deposition of nanoparticles on and inside the sulfonated nanospheres. Furthermore, elemental mapping images (**Figure 2K-M)** further confirmed that the nanoparticles were growing outside and inside of the HCNs. Whereas, without the support of SPS templates, only aggregated solid ZnSe MSs were obtained with various diameters ranging from 200 nm to 8 μm (**Figure S2**, see Supporting Information). The Energy Dispersive X-ray (EDX) spectroscopy results (**Figure S3A**, see Supporting Information) of ZnSe@HCNs detected three elements: Zn, Se and C in the hybrid structure, with the atomic ratio of Zn/Se close to 1:1, indicating the nanoparticles are ZnSe of almost the stoichiometric composition. While only Zn and Se elements are found in aggregated ZnSe MSs samples (**Figure S3B**, see Supporting Information).

The crystallinity of the hybrid composite was investigated using X-ray diffraction (XRD), high-resolution TEM (HRTEM) and selected area electron diffraction (SAED) techniques. **Figure S4** (Supporting Information) shows the XRD pattern of the ZnSe@HCNs and the ZnSe MSs samples. All the peaks can be assigned to the stilleite ZnSe crystal structure peaks (JCPDS 88-2345), demonstrating the high crystallinity and purity of the composites.[37] **Figure S5** (see Supporting Information) further discloses the corresponding refined structural model along different orientation. Similar to previously reported literature, the crystal structure of stilleite ZnSe is consisted by [$ZnSe_4$] stacks.[38] Along the [110] direction, pyramidal [$ZnSe_4$] units exhibit an individual vertex-sharing chains array to form a tunnel structure with a 2.487 Å edge length, providing adequate space to accommodate Na^+ ions (1.02 Å) during the electrochemical process. The HRTEM image of the ZnSe@HCNs in **Figure 2H** shows an interplanar distance of 0.327 mm, corresponding to the dominant (111) facet. The selected area electron diffraction (SAED) pattern (**Figure 2I**) reveals a polycrystalline feature and the intense diffraction rings are readily indexed to cubic ZnSe crystalline, in good agreement with the above XRD results.

Furthermore, the total carbon content was calculated from the thermogravimetric analysis (TGA) curves to be 23.0 wt% in the ZnSe@HCNs composites (**Figure S6**, see Supporting Information). The typical Raman spectra of ZnSe@HCNs, HCNs and aggregated ZnSe MSs are shown in **Figure S7** (see Supporting Information). The Raman spectra of ZnSe@HCNs and HCNs show two bands centred at 1337 and 1598 cm^{-1}, corresponding to the disordered amorphous carbon (D band) and the crystalline graphitic carbon (G band), respectively. Also, two intensive Raman peaks at about 202 and 249 cm^{-1} on the Raman plots of ZnSe@HCNs and aggregated ZnSe MSs can also be detected distinctly, which are well indexed to the representative 1LO bands of ZnSe phase. The chemical composition and valence states of the as-prepared ZnSe@HCNs were detected by X-ray photoelectron spectra (XPS) (**Figure S8**, see Supporting Information). The survey scan spectrum indicates the presence of Zn, Se and C elements (**Figure S8A**). The high-resolution spectrum of the Se 3d (**Figure S8B**) shows two dominant peaks located at 55.2 eV and 54.4 eV corresponding to Se $3d_{3/2}$, and Se $3d_{5/2}$, respectively, suggesting the presence of Se^{2-}.[39] The Zn 2p high-resolution XPS spectrum (**Figure S8C**) also demonstrates the characteristic signals of Zn $2p_{1/2}$ peak at 1045.2 eV and Zn $2p_{3/2}$ peak at 1022.1 eV, confirming the valence state of Zn^{2+}.[11] The high-resolution C 1s spectrum (**Figure S8D**) can be divided into three components: C-C peak at 284.8 eV, C-O peak at 285.7 eV and C=O peak at 287.4 eV. The detection of carbon-oxygen bonds suggests that ZnSe nanoparticles are linked chemically to the carbon spheres through some oxygen functional groups. The pore structure and the surface area of the ZnSe@HCNs hybrid were evaluated by the N_2 adsorption/desorption analysis in **Figure S9A** (see Supporting Information). The distinct hysteresis loops between the adsorption and desorption curves of ZnSe@HCNs in the medium to high-pressure regions (P/P_0 range 0.4-1.0) is typical for type IV isotherm.[35] The pore size distribution (**Figure S9B**) shows that the mesopores peaked at ~2.2 nm. The calculated Brunauer-Emmert-Teller (BET) surface area of the of the ZnSe@HCNs is 241.9 m^2 g^{-1}. This value is five times higher than the aggregated sample, indicating the success of synthesising a porous structure by directing and controlling the deposition of ZnSe nanoparticles. Such larger surface area can highly increase the surface and near-surface reactions of active materials during the discharge/charge process, thus guaranteeing the excellent electrochemical performance of the ZnSe@HCNs.[40]

To distinguish the density difference of as-prepared ZnSe@HCNs and HCNs, we filled their powder in a quartz tube respectively with an inside diameter of 4 mm (**Figure S10A**, see Supporting Information). As a result, the filled length of tube (i) with 0.4 g of ZnSe@HCNs powder is about 5.4 cm, while the filled length of tube (ii) with the same mass HCNs reaches to 6.7 cm, implying the tap density of ZnSe@HCNs higher than that of HCNs since the density ratio of ZnSe@HCNs to HCNs is around 1.24:1. Namely, the density of HCNs is highly enhanced after growing some fine ZnSe nanoparticles on their outer/inner surfaces. In order to further calculate the tap density of ZnSe@HCNs and HCNs, respectively, we pasted them on Cu foil with a diameter of 12.6 mm and conducted the FESEM observation to verify the thickness of active layer as shown in **Figure S10B** and **S10C** (see Supporting Information). And the corresponding data are listed in **Table S2** (see Supporting Information). After calculated, the tap densities of ZnSe@HCNs and HCNs are about 1.38 and 1.08 g cm^{-3}, respectively. The ZnSe@HCNs possesses higher tap density than pure HCNs, disclosing our fabrication strategy can improve the tap density of hollow carbon materials through growing fine ZnSe nanoparticles onto the outer and inner interfaces of HCNs.

Subsequently, we investigated the electrochemical performance of the ZnSe@HCNs hybrid in two-electrode configurations. **Figure 3A** reveals the galvanostatic discharge and charge profiles of the ZnSe@HCNs cycled at a constant current density of 1.0 A g^{-1}. The initial discharge and charge capacities are 445.6 and 410.7 mAh g^{-1}, respectively, yielding a high initial Coulombic efficiency of 92.2 %. The irreversible capacity loss (about 7.8%) in the first cycle is attributed to the irreversible decomposition of electrolyte and the formation of the solid-electrolyte interface (SEI) layer.[41] Similar to other metal selenides like $CoSe_2$ and $FeSe_2$, the initial discharge and charge profiles are far different from the following ones.[4, 18, 42] The formation of SEI layer is not only the irreversible reaction in the initial cycles, but some other side reactions resulted from the activation of the selenides, which make the initial sodiation and desodiation processes unstable.[43] To bring more insights on the electrochemical sodiation and desodiation mechanism, we further used cyclic voltammetry (CV) techniques. The representative CV profiles of ZnSe@HCNs recorded for the 1st, 2nd and 5th cycles are shown in **Figure S11** (see Supporting Information). In the first cathodic scan, a strong reduction peak at 0.30 V and a weak reduction peak at 0.92 V are observed. The corresponding anodic scan shows three oxidation peaks in the first cycle at 0.90 V, 1.56 and 1.92 V. These CV results are in good accordance with the initial discharge/charge platforms. After the first cycle, the ZnSe@HCNs electrodes undergo a series of complicated activation processes. Three discharge platforms at round 1.58, 0.94 and 0.62 V and two charge platforms at about 1.51 and 1.85 V can be maintained after 100 cycles. **Figure 3B** reveals long-term cycle stability of ZnSe@HCNs. Benefiting from the unique hierarchical nanostructure, the ZnSe@HCNs show an excellent cycle stability. Even after 1000 cycles at 1.0 and 10.0 A g^{-1}, the ZnSe@HCNs electrodes can still deliver high reversible discharge capacities of 361.9 and 285.9 mAh g^{-1}, respectively, corresponding to a high capacity retention of 87.0% of the second cycle (for 1.0 A g^{-1}). However, without the support of

HCNs, the solid ZnSe MSs anodes reveal inferior electrochemical performance. As shown in **Figure S12A** (see Supporting Information), the discharge capacity decreases sharply from 349.4 to 198.2 mAh g^{-1} after 550 cycles at 1.0 A g^{-1}. The activation process of solid ZnSe MSs electrodes need more than 150 discharge/charge cycles, thus leading to much sluggish voltage platform transformation especially on the charge branches (**Figure S12B**, see Supporting Information).

We further investigated the rate performance of the ZnSe@HCNs hybrid electrode at various current densities ranging from 0.2 to 20.0 A g^{-1}. As shown in **Figure 3C**, the ZnSe@HCNs anodes provide excellent high-rate capability and stable Coulombic efficiency of about 98.7%. With the current density gradually increasing from 0.2 to 20.0 A g^{-1}, the reversible discharge capacity decreases from 484.2 to 264.1 mAh g^{-1}, respectively. Interestingly, once the current densities come back to 10.0 and 1.0 A g^{-1} after more than 40 cycles, the corresponding discharge capacities can be rapidly recovered to 340.1 and 444.5 mAh g^{-1}, respectively. The detailed discharge/charge profiles of the ZnSe@HCNs at different current densities are presented in **Figure S13** (see Supporting Information). On the other hand, the solid aggregated ZnSe MSs demonstrate poor rate performance with lower discharge capacity and unsteady Coulombic efficiency (**Figure S14**, see Supporting Information). To highlight the outstanding high-rate performance of the ZnSe@HCNs, the discharge capacities of other reported metal selenides at different current densities are summarized in **Figure 3D** and **Table S3** (see Supporting Information). [4, 9, 12-15, 17, 19, 22, 24, 42, 44-47] The ZnSe@HCNs hybrid anode demonstrates a more competitive rate capability with high reversible discharge capacity than reported metal selenides, particularly at higher current densities. Such higher capacity retention of the ZnSe@HCNs anode can be attributed to the abundant surface and near-surface reactions since there are numerous ultrafine ZnSe particles firmly anchored on/in the HCNs.[48-49] Also, the conductive and flexible HCNs backbone ensures faster electrons/ions transport, more sufficient electrolyte-electrode contact area and more beneficial structure buffer.[50] It should be noted that the capacity contribution of pure HCNs is meagre, and could be omitted when calculating the total discharge capacity of the ZnSe@HCNs. As shown in **Figure S15** (see Supporting Information), the pure HCNs can only deliver a low discharge capacity of about 18 mA g^{-1} at 1.0 A g^{-1}.

The high-rate performance of electrode materials is related to the potential pseudocapacitive behaviour upon the continuous discharge/charge cycling.[50] To explore the electrochemical reaction dynamics, we further measured the CV curves of both ZnSe@HCNs and ZnSe MSs at various scan rates from 0.2 to 1.0 mV s^{-1}. The corresponding results are presented in **Figure 3E** and **Figure S16** (see Supporting Information). Generally, the peak current (i) and the scan rate (v) obey the following equations:[51]

$$i = av^{b} \qquad (1)$$

$$\log(i) = b\cdot\log(v) + \log(a) \qquad (2)$$

where a and b stand for the adjustable parameters, and b value is determined from the slope of log(i) vs. log(v) plot. The value of b gives a good indication of the determining step of the electrochemical process. Usually, when b is equal to 0.5, the electrochemical sodium storage reaction is controlled by the ionic diffusion. While when b approaches to 1.0, the sodium storage process is dominated by pseudocapacitance.[52] As shown in **Figure 3F**, the b-values (fitted slopes) of seven peaks are ranged between 0.7 to 1.04, suggesting a mixed process with the surface controlled pseudocapacitive process as the predominant mechanism on the ZnSe@HCNs. Furthermore, we have calculated the pseudocapacitive contribution from the equation: $i = k_1v + k_2v^{0.5}$, where k_1v and $k_2v^{0.5}$ represent the pseudocapacitive and ionic diffusion contributions, respectively.[4] **Figure 3G** shows the calculated pseudocapacitive contributions of ZnSe@HCNs anode gradually increase from 70.9% to 85.5% at the scan rates growing from 0.2 to 1.0 mV s^{-1}. The unique design of the electrode materials plays a major role of minimising the diffusion limitation, particularly in the high scan rate. The open structure leads to the fast Na^+ intercalation/extraction and durable cyclic stability, thus facilitating the high-rate and long-term cycle performance of as-prepared ZnSe@HCNs. For instance, the detailed pseudocapacitive fraction at 1.0 mV s^{-1} is demonstrated in **Figure 3H**. This result is analogous to the case of other metal sulfides/selenides.[26, 53]

In addition to the pseudocapacitance storage mechanism, there is also a possibility for slower redox reactions that could take place in the anode. Conversion reactions and alloying reaction are commonly reported for most anode materials in SIBs. These types of reactions are usually associated with more serious structural changes than the changes associated with the pseudocapacitive storage. To study the phase changes during the discharge and charge, ex-situ XRD, SAED and HRTEM were performed at different stages. **Figure 4A** presents the ex-situ XRD patterns at various discharge/charge stages. The typical diffraction peaks of the cubic ZnSe diminish gradually and disappear completely with the discharge voltage decreasing from 1.5 V to 0.1 V. In the meantime, the weak diffraction peaks of Zn and Na_2Se can be detected when the discharge voltages attenuate to 1.0 and 0.4 V. After fully discharged to 0.1 V, some new characteristic peaks located at 32.4°, 35.6° and 69.6° emerge, which can be assigned to the (420), (422) and (753) crystal planes of cubic $NaZn_{13}$ phase (JPCDF no. 03-1008), confirming the presence of $NaZn_{13}$ alloy in the final discharge products.[28, 29] During the subsequent charge process, the strong characteristic diffraction peaks of ZnSe are recovered gradually, and the diffraction peaks of Zn, Na_2Se and $NaZn_{13}$ vanish completely. Also, the intermediates were verified further by ex-situ SADE and HRTEM images. As shown in **Figure 4C**, the hierarchical hybrid structure of the ZnSe@HCNs still can be well retained when the fresh cell was discharged to 0.2 V. The ex-situ SADE (**Figure 4D**) clearly discloses the polycrystalline diffraction rings of (111) and (220) planes of Na_2Se, (420) plane of $NaZn_{13}$, and (101) plane of Zn. Besides, the lattice fringes of these discharge intermediates are also found in **Figure 4E**. After the tested cell was charged to 2.6 V once again (**Figure 4F**), the distinct structural changes of the ZnSe@HCNs hardly happen, confirming the robust hybrid structure of the ZnSe@HCNs. The ex-situ SADE (**Figure 4G**) and ex-situ HRTEM (**Figure 4H**) reveal the typical diffraction rings and lattice fringes of (111) and (220) planes of ZnSe, respectively, indicating the main charge product is ZnSe. Therefore, based on the above results, the phase changes of the ZnSe@HCNs electrode materials are governed by the following equations:

Conversion reactions: $ZnSe + 2Na^+ + 2e^- \leftrightarrow Na_2Se + Zn$ (3)

Alloying/dealloying reaction: $13Zn + Na^+ + e^- \leftrightarrow NaZn_{13}$ (4)

It should be mentioned here that detecting these phases changes does not exclude the storage via the pseudocapacitive process, which usually limited to the surface and do not cause severe structural changes. Also, from a pure kinetic point of view, the small particle size of the ZnSe in the novel open ZnSe@HCNs structure shorten the diffusion pathway, and hence the constant b in equations 1 and 2 are shifted toward more diffusion independent values. The theoretical capacity calculated based on reactions (3) and (4) is 402.9 mAh g^{-1} while the recorded value for the ZnSe@HCNs reveals a higher capacity of 484.2 mAh g^{-1} at 0.2 A g^{-1}, clearly confirming the role of the pseudocapacitive contribution.

It is well known that the electrolyte plays a significant role in determining the electrochemical performance of SIBs.[42] Thus, we have compared the ether-based electrolyte (1.0 M $NaCF_3SO_3$ in diethylene glycol dimethyl ether (DEGDME)) with two kinds of carbonate-based electrolytes; (i) 1.0 M $NaClO_4$ in propylene carbonate (PC) with 5 wt% fluoroethylene carbonate (FEC); and (ii) 1.0 M $NaPF_6$ in ethylene carbonate/dimethyl carbonate (EC/DEC; v/v=1:1). We first carried out electrochemical impedance spectroscopy (EIS) measurements for half-cells using the different electrolytes and the ZnSe@HCNs electrodes. The ether-based electrolyte possesses the lowest charge-transfer resistance, thus efficiently enhancing the electrochemical reaction kinetics of the ZnSe@HCNs (**Figure S17**, see Supporting Information). Also, the contact angle measurements also reveal that ether-based electrolyte processes better wettability than carbonate-based electrolytes (**Figure S18**, see Supporting Information), which is expected to facilitate the reactions on the electrode/electrolyte interface. The electrochemical cyclic performance of the ZnSe@HCNs electrode in the three different electrolytes is shown in F**igure S19** (see Supporting Information). As expected, the cells with carbonate-based electrolytes suffer from severe capacity decay. For example, when using 1.0 M $NaClO_4$ in PC with 5 wt% FEC as the electrolyte, the initial discharge capacity of the ZnSe@HCNs electrode was about 400 mAh g^{-1}, and it decreased quickly to 95 mAh g^{-1} after 100 cycles at 1 A g^{-1}. The performance of the cell with 1.0 M $NaPF_6$ in DC/DEC (v/v, 1:1) electrolyte showed slightly better performance, but the discharge capacity was still low after 100 cycles (170.0 mAh g^{-1}). **Figure 5A** schematically illustrates the sodiation and desodiation process of hybrid ZnSe@HCNs. As shown in **Figure 5B**, the ZnSe@HCNs still maintain their conformal hybrid structure even after 500 cycles at 1.0 A g^{-1}. No apparent structural collapse or severe pulveriation can be observed, benefiting from the support and confinement of flexible HCNs to ultrafine ZnSe particles. Nevertheless, the aggregated solid ZnSe MSs suffer from serious structural collapse and pulverization (**Figure 5C**). The EIS measurements of above two samples were also conducted. The impedance of ZnSe MSs samples reveal an obvious increase after 500 cycles, indicating undesirable cycling performance (**Figure 5D-E**).

Inspired by the excellent electrochemical performance of the Na//ZnSe@HCNs half-cell, we further constructed sodium-ion full cells using $Na_3V_2(PO_4)_3$ (NVP) as the cathode. **Figure 6A** schematically illustrates the structure and composition of the NVP//ZnSe@HCNs full cells. The selection of NVP was based on its excellent performance in SIBs.[54] In this research, NVP microflowers were firstly synthesised via a hydrothermal process.[55] The phase purity of the prepared NVP was confirmed by XRD analysis and the morphology was investigated by SEM images (**Figure S20**, see Supporting Information). We first investigated the NVP cathode in a half-cell, which exhibits a stable reversible discharge capacity of about 104.7 mAh g^{-1} after 100 cycles at 1C (1C=117 mA g^{-1}). Then we evaluated the performance of the NVP//ZnSe@HCNs full cells. The initial three galvanostatic discharge and charge voltage profiles of the full cell cycled at 0.5 A g^{-1} between 0.1 and 3.0 V are displayed in **Figure 6B**. Remarkably, the full cell has a Coulombic efficiency of about 98.2% and can deliver a stable reversible discharge capacity of about 313.1 mAh

g^{-1} after 100 cycles at the current density of 0.5 A g^{-1} (**Figure 6C**), providing more evidence of the potential of the ZnSe@HCNs as anodes for high-performance sodium ion batteries.

4. Conclusion

In summary, we successfully developed a novel hierarchical hybrid nanostructure of ultrafine ZnSe particles growing on/in hollow carbon nanospheres derived from the carbonation of SPS spheres (ZnSe@HCNs) as a promising anode for SIBs for the first time. In this tailored structure, the SPS templates can absorb ultrafine ZnSe precursor particles both on/in their surface, significantly inhibiting the volume expansion during the repeated sodiation and desodiation process. When used as anodes for SIBs in the ether-based electrolyte, the ZnSe@HCNs exhibits a high reversible capacity of 361.9 and 285.9 mAh g^{-1} at 1 and 10 A g^{-1} after 1000 cycles, respectively. Thanks to the enhanced surface and near-surface reactions along with the high pseudocapacitive behaviours of ZnSe@HCNs samples, a remarkable rate performance is achieved as well (264.0 mAh g^{-1} at 20 A g^{-1}). In addition, we further demonstrate that the ZnSe@HCNs could be coupled with NVP to assemble full batteries, which also delivers a specific discharge capacity of 313.1 mAh g^{-1}. Above results provide a new strategy to construct nanosized transition-metal chalcogenides, phosphides or alloys with carbon matrix, revealing highly enhanced sodium ion storage.

Acknowledgements

This research was supported partially by the Key Laboratory Construction Program of Xi'an Municipal Bureau of Science and Technology (201805056ZD7CG40), Project of National Defense Science and Technology Innovation Special Zone (JZ-20171102), National Natural Science Foundation of China (No. 51773165), China Postdoctoral Science Foundation (No. 2016M592776), Natural Science Foundation of Shaanxi Province (No. 2016JM5021) and Postdoctoral Science Foundation of Shaanxi Province (No. 2016BSHYDZZ20). The authors would like to thank the

Center for Advancing Materials Performance from the Nanoscale (CAMP-Nano) for allowing the use of field-emission scanning electron microscopy. We also thank Mr Gang Chang and Miss Jiao Li at Instrument Analysis Center of Xi’an Jiaotong University for their assistance with BET and TEM Mapping analysis.

Appendix A. Supplementary material

Supplementary data associated with this article can be found in the online version at

References

[1] Y. Y. Liu, G. M. Zhou, K. Liu, Y. Cui, Acc. Chem. Res. 50 (2017) 2895-2905.

[2] A. Manthiram, X. W. Yu, S. F. Wang, Nat. Rev. Mater. 2 (2017) 16103.

[3] S. Y. Lu, T. X. Zhu, Z. Y. Li, Y. C. Pang, L. Shi, S. J. Ding, G. X. Gao, J. Mater. Chem. A. 6 (2018) 7005-7013.

[4] K. Zhang, M. H. Park, L. M. Zhou, G.-H. Lee, W. J. Li, Y.-M. Kang, J. Chen, Adv. Funct. Mater. 26 (2016) 6728-6735.

[5] Y. M. Sun, N. Liu, Y. Cui, Nat. Energy 1 (2016) 16071.

[6] J. Y. Hwang, S. T. Myung, Y. K. Sun, Chem. Soc. Rev. 46 (2017) 3529-3614.

[7] J. Q. Deng, W. B. Luo, S. L. Chou, H. K. Liu, S. X. Dou, Adv. Energy Mater. 8 (2018) 1701428.

[8] H. Kim, H. Kim, Z. Ding, M. H. Lee, K. Lim, G. Yoon, K. Kang, Adv. Energy Mater. 6 (2016) 1600943.

[9] J. Yang, Y. F. Zhang, Y. Z. Zhang, J. J. Shao, H. B. Geng, Y. Zhang, Y. Zheng, M. Ulaganathan, Z. F. Dai, B. Li, Y. Zong, X. C. Dong, Q. Y. Yan, W. Huang, Small. 13 (2017) 1702181.

[10] J. Deng, Q. F. Gong, H. L. Ye, K. Feng, J. H. Zhou, C. Y. Zha, J. H. Wu, J. M. Chen, J. Zhong, Y. G. Li, ACS Nano. 12 (2018) 1829-1836.

[11] M. J. Jing, Z. G. Chen, Z. Li, F. Y. Li, M. J. Chen, M. J. Zhou, B. H. He, L. Chen, Z. H. Hou, X. B. Chen, ACS Appl. Mater. Interfaces. 10 (2018) 704-712.

[12] Q. H. Wang, W. C. Zhang, C. Guo, Y. J. Liu, C. Wang, Z. P. Guo, Adv. Funct. Mater. 27 (2017) 1703390.

[13] C. Wu, P. Kopold, P. A. van Aken, J. Maier, Y. Yu, Adv. Mater. 29 (2017) 1604015.

[14] J. Qin, T. S. Wang, D. Y. Liu, E. Z. Liu, N. Q. Zhao, C. S. Shi, F. He, L. Y. Ma, C. N. He, Adv. Mater. 30 (2018) 1704670.

[15] Z. A. Zhang, X. D. Shi, X. Yang, Y. Fu, K. Zhang, Y. Q. Lai, J. Li, ACS Appl. Mater. Interfaces. 8 (2016) 13849-13856.

[16] X. Ou, C. H. Yang, X. H. Xiong, F. H. Zheng, Q. C. Pan, C. Jin, M. L. Liu, K. Huang, Adv. Funct. Mater. 27 (2017) 1606242.

[17] F. Niu, J. Yang, N. N. Wang, D. P. Zhang, W. L. Fan, J. Yang, Y. T. Qian, Adv. Funct. Mater. 27 (2017)

1700522.

[18] Y. C. Tang, Z. B. Zhao, X. J. Hao, Y. W. Wang, Y. Liu, Y. N. Hou, Q. Yang, X. Z. Wang, J. S. Qiu, J. Mater. Chem. A. 5 (2017) 13591-13600.

[19] S. H. Zhu, Q. D. Li, Q. L. Wei, R. M. Sun, X. Q. Liu, Q. Y. An, L. Q. Mai, ACS Appl. Mater. Interfaces. 9 (2017) 311-316.

[20] X. Ou, J. Li, F. H. Zheng, P. Wu, Q. C. Pan, X. H. Xiong, C. H. Yang, M. L. Liu, J. Power Sources. 343 (2017) 483-491.

[21] S.-K. Park, J. K. Kim, Y. Chan Kang, J. Mater. Chem. A. 5 (2017) 18823-18830.

[22] F. Zhang, C. Xia, J. J. Zhu, B. Ahmed, H. F. Liang, D. B. Velusamy, U. Schwingenschlögl, H. N. Alshareef, Adv. Energy Mater. 6 (2016) 1601188.

[23] Z. Hu, Q. N. Liu, S. L. Chou, S. X. Dou, Adv. Mater. 29 (2017) 1700606.

[24] C. Wu, Y. Jiang, P. Kopold, P. A. van Aken, J. Maier, Y. Yu, Adv. Mater. 28 (2016) 7276-7283.

[25] S. Q. Chen, L. F. Shen, P. A. van Aken, J. Maier, Y. Yu, Adv. Mater. 29 (2017) 1605650.

[26] Y. J. Fang, X. Y. Yu, X. W. Lou, Adv. Mater. 30 (2018) 1706668.

[27] H. Liu, H. Guo, B. H. Liu, M. F. Liang, Z. L. Lv, K. R. Adair, X. L. Sun, Adv. Funct. Mater. 28 (2018) 1707480.

[28] S. H. Dong, C. X. Li, X. L. Ge, Z. Q. Li, X. G. Miao, L. W. Yin, ACS Nano. 11 (2017) 6474-6482.

[29] G. Z. Fang, Z. X. Wu, J. Zhou, C. Y. Zhu, X. X. Cao, T. Q. Lin, Y. M. Chen, C. Wang, A. Q. Pan, S. Q. Liang, Adv. Energy Mater. 8 (2018) 1703155.

[30] S. Vasilyev, I. Moskalev, M. Mirov, S. Mirov, V. Gapontsev, Opt. Express. 24 (2016) 1616-1623.

[31] S. Kim, A. R. Marshall, D. M. Kroupa, E. M. Miller, J. M. Luther, S. Jeong, M. C. Beard, ACS Nano. 9 (2015) 8157-8164.

[32] W. J. Yang, B. D. Liu, B. Yang, J. Y. Wang, T. Sekiguchi, S. Thorsten, X. Jiang, Adv. Funct. Mater. 25 (2015) 2543-2551.

[33] Z. L. Chen, R. B. Wu, H. Wang, K. H. L. Zhang, Y. Song, F. L. Wu, F. Fang, D. L. Sun, Nano Res. 11 (2017) 966-978.

[34] Y. H. Xu, J. W. Liang, K. L. Zhang, Y. C. Zhu, D. H. Wei, Y. T. Qian, Electrochem. Commun. 65 (2016) 44-47.

[35] C. J. Tang, X. J. Wei, X. Y. Cai, Q. Y. An, P. Hu, J. Z. Sheng, J. X. Zhu, S. L. Chou, L. M. Wu, L. Q. Mai, ACS Appl. Mater. Interfaces. 10 (2018) 19626-19632.

[36] Y. K. Wang, R. F. Zhang, Y. C. Pang, X. Chen, J. X. Lang, J. J. Xu, C. H. Xiao, H. L. Li, K. Xi, S. J. Ding, Energy Storage Mater. 16 (2019) 228-235.

[37] Z. A. Zhang, Y. Fu, X. Yang, Y. H. Qu, Q. Li, Electrochim. Acta. 168 (2015) 285-291.

[38] D. W. Su, K. Kretschmer, G. X. Wang, Adv. Energy Mater. 6 (2016) 1501785.

[39] M. Wan, R. Zeng, K. Y. Chen, G. X. Liu, W. L. Chen, L. L. Wang, N. Zhang, L. H. Xue, W. X. Zhang, Y. H. Huang, Energy Storage Mater. 10 (2018) 114-121.

[40] C. T. Zhao, C. Yu, B. Qiu, S. Zhou, M. D. Zhang, H. W. Huang, B. Q. Wang, J. J. Zhao, X. L. Sun, J. S. Qiu, Adv. Mater. 30 (2018) 1702486.

[41] S. Y. Lu, Y. Y. Gao, Z. Y. Li, B. T. Dong, T. Gao, S. J. Ding, Y. Bai, G. X. Gao, J. Alloys Comp. 749 (2018)

424-432.

[42] K. Zhang, Z. Hu, X. Liu, Z. L. Tao, J. Chen, Adv. Mater. 27 (2015) 3305-3309.

[43] X. Chen, X. Shen, B. Li, H. J. Peng, X. B. Cheng, B. Q. Li, X. Q. Zhang, J. Q. Huang, Q. Zhang, Angew. Chem. Int. Ed. 57 (2018) 734-737.

[44] X. Xu, R. Zhao, W. Ai, B. Chen, H. Du, L. Wu, H. Zhang, W. Huang, T. Yu, Adv. Mater. 30 (2018) 1800658.

[45] P. He, Y. Fang, X. Y. Yu, X. W. D. Lou, Angew. Chem. Int. Ed. 56 (2017) 12202-12205.

[46] X. Wang, K. Chen, G. Wang, X. Liu, H. Wang, ACS Nano 11 (2017) 11602-11616.

[47] S. Yao, J. Cui, Z. Lu, Z. L. Xu, L. Qin, J. Huang, Z. Sadighi, F. Ciucci, J. K. Kim, Adv. Energy Mater. 7 (2017) 1602149.

[48] X. Han, G. He, Y. He, J. Zhang, X. Zheng, L. Li, C. Zhong, W. Hu, Y. Deng, T. Y. Ma, Adv. Energy Mater. 8 (2018) 1702222.

[49] H. Li, Y. Sun, Z. Y. Yuan, Y. P. Zhu, T. Y. Ma, Angew. Chem. Int. Ed. 57 (2018) 3222-3227.

[50] V. Augustyn, P. Simon, B. Dunn, Energy Environ. Sci. 7 (2014) 1597-1614.

[51] P. Ge, C. Y. Zhang, H. S. Hou, B. K. Wu, L. Zhou, S. J. Li, T. J. Wu, J. G. Hu, L. Q. Mai, X. B. Ji, Nano Energy. 48 (2018) 617-629.

[52] X. M. Yang, H. K. Wang, D. Y. W. Yu, A. L. Rogach, Adv. Funct. Mater. 28 (2018) 1706609.

[53] D. H. Liu, W. H. Li, Y. P. Zheng, Z. Cui, X. Yan, D. S. Liu, J. W. Wang, Y. Zhang, H. Y. Lü, F. Y. Bai, J. Z. G, X. L. W. Adv. Mater. 30 (2018) 1706317.

[54] Y. Jiang, Z. Z. Yang, W. H. Li, L. C. Zeng, F. S. Pan, M. Wang, X. Wei, G. T. Hu, L. Gu, Y. Yu, Adv. Energy Mater. 5 (2015) 1402104.

[55] Q. Y. An, F. Y. Xiong, Q. L. Wei, J. Z. Sheng, L. He, D. L. Ma, Y. Yao, L. Q. Mai, Adv. Energy Mater. 5 (2015) 1401963.

Figures

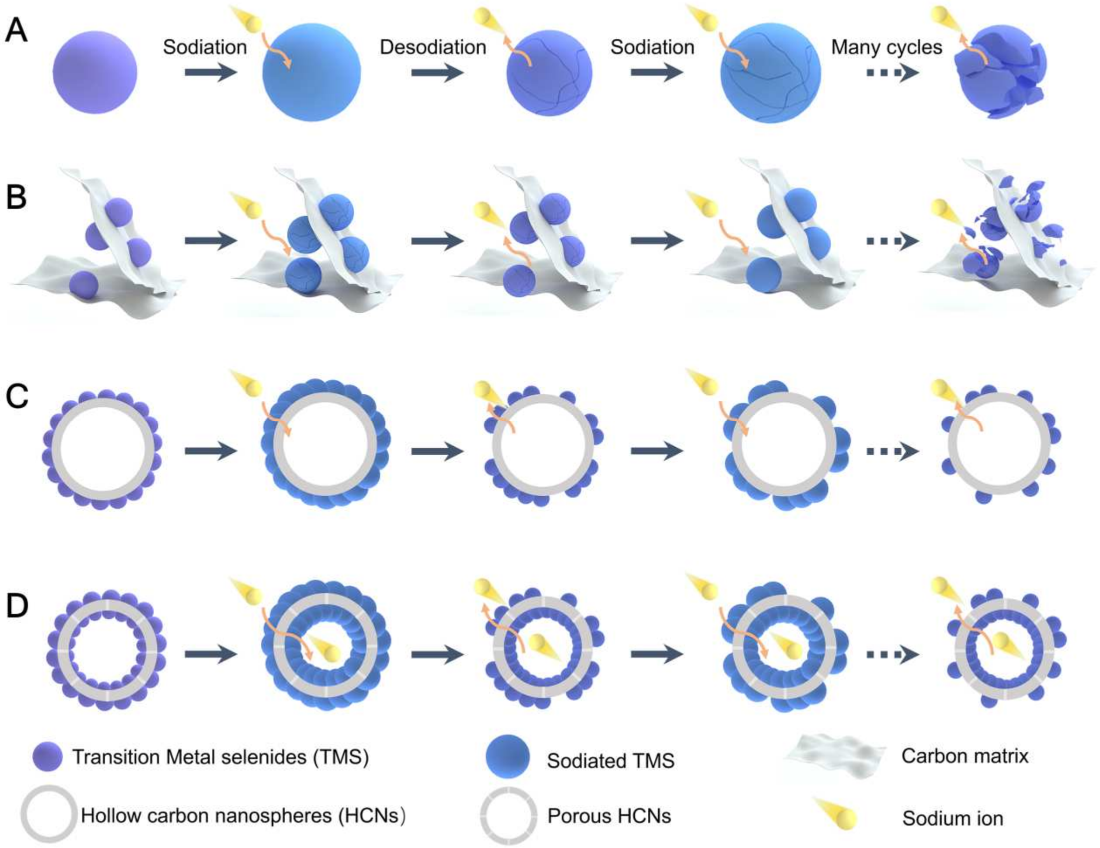

Figure 1. Schematic illustration of the morphology evolutions of transition metal selenide (TMS) composites after many cycles. (A) Bare TMS, (B) TMS with carbon matrix, (C) TMS on hollow carbon nanospheres, (D) TMS on/in porous hollow carbon nanopsheres.

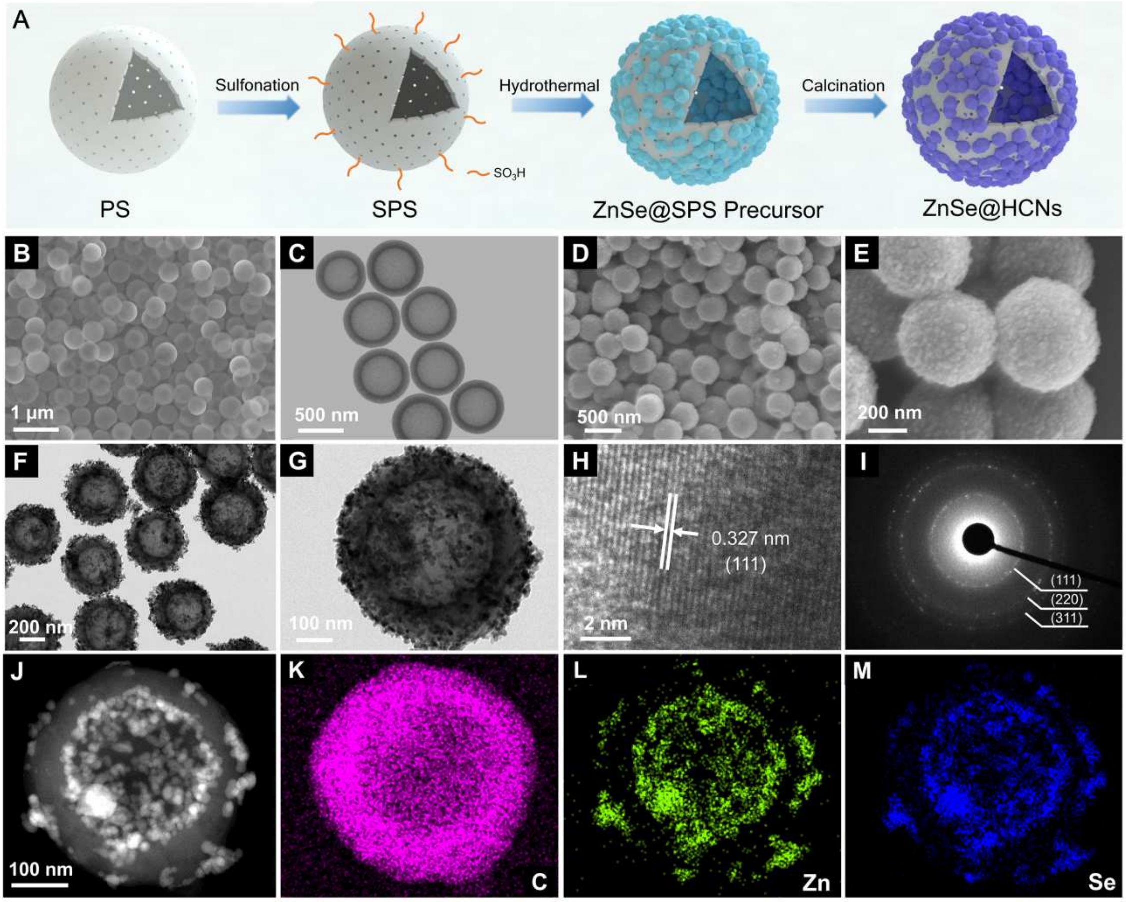

Figure 2. (A) Schematic illustration of the formation of hybrid ZnSe@HCNs; (B) FESEM and (C) TEM images of SPS templates; (D-E) FESEM, (F-G) TEM, (H) HRTEM, (I) SEAD images, (J) HAADF-STEM image and (K-M) corresponding elemental mapping images of hybrid ZnSe@HCNs.

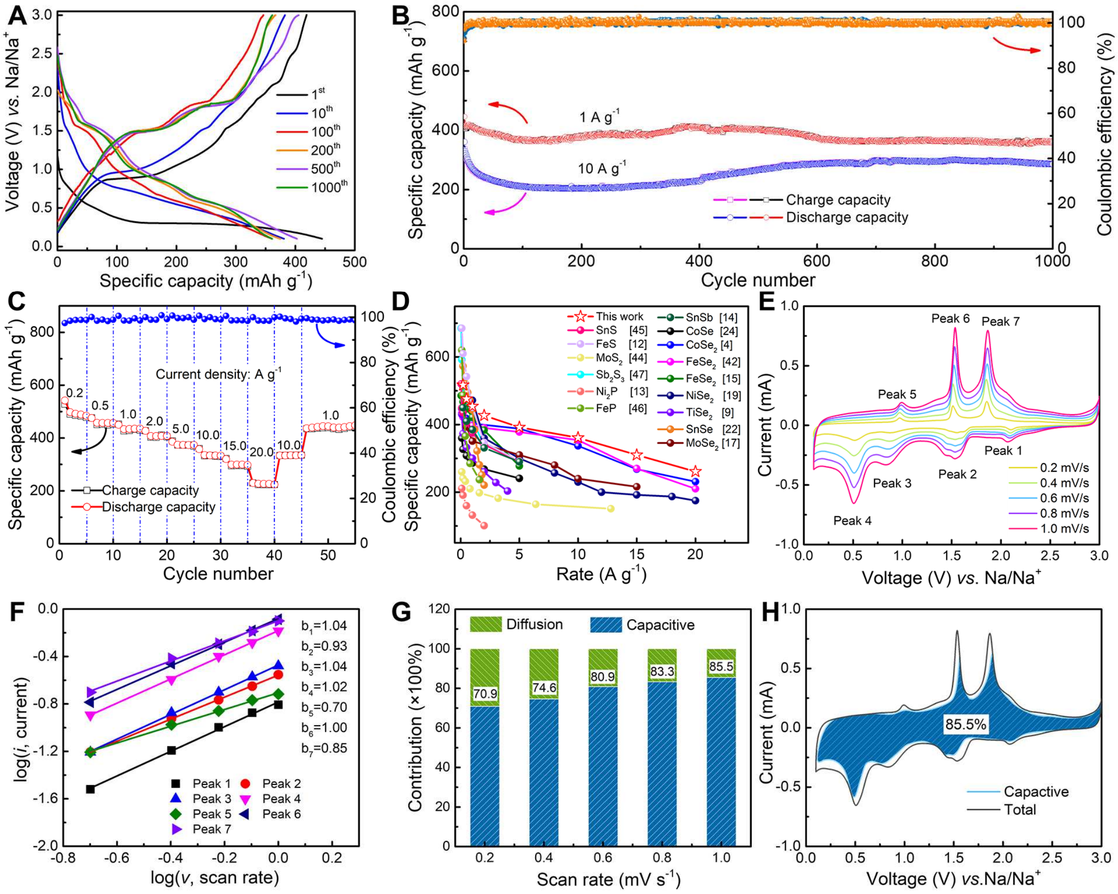

Figure 3. Electrochemical performance of ZnSe@HCNs in the cut-off voltage of 0.1-3.0 V: (A) Charge-discharge curves at 1.0 A g^{-1} with different cycles, (B) Cyclic stability at 1.0 and 10.0 A g^{-1}, (C) Rate capability evaluated at various current densities ranging from 0.2 to 20.0 A g^{-1}, (D) Comparison of rate performance with other typical anode materials for SIBs, (E) CV profiles at different scan rates, (F) Corresponding log *i* versus log *v* plot at each redox peak, (G) Percent of pseudocapacitive contribution at different scan rates, (H) CV curve with pseudocapacitive fraction shown by blue region at a scan rate of 1 mV s^{-1}.

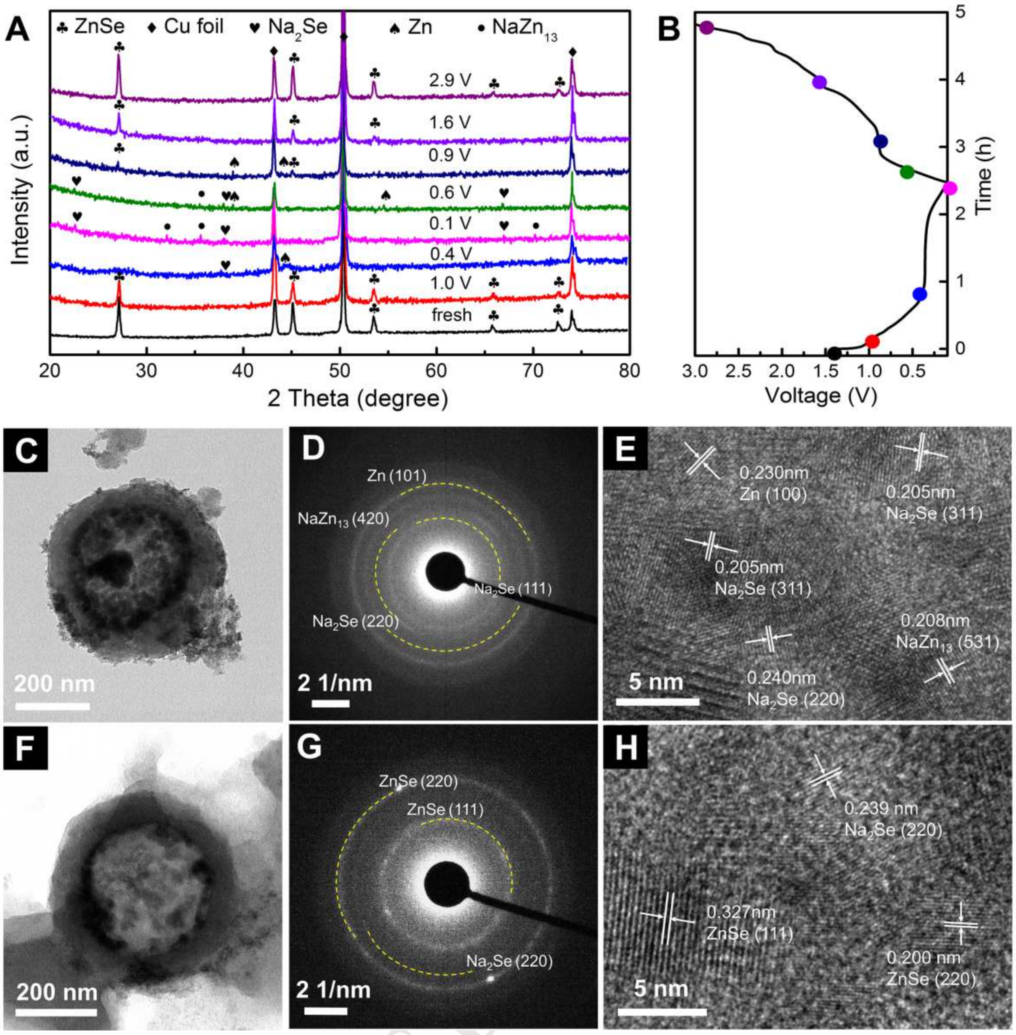

Figure 4. Electrochemical reaction mechanism: (A) Ex-situ XRD analysis of the ZnSe@HCNs electrodes at different charge/discharge states and (B) Corresponding charge/discharge curve, (C, F) Ex-situ TEM, (D, G) SADE and (E, H) HRTEM of ZnSe@HCNs at different cycling states: (C-E) discharge to 0.2 V, (F-H) charge to 2.6 V.

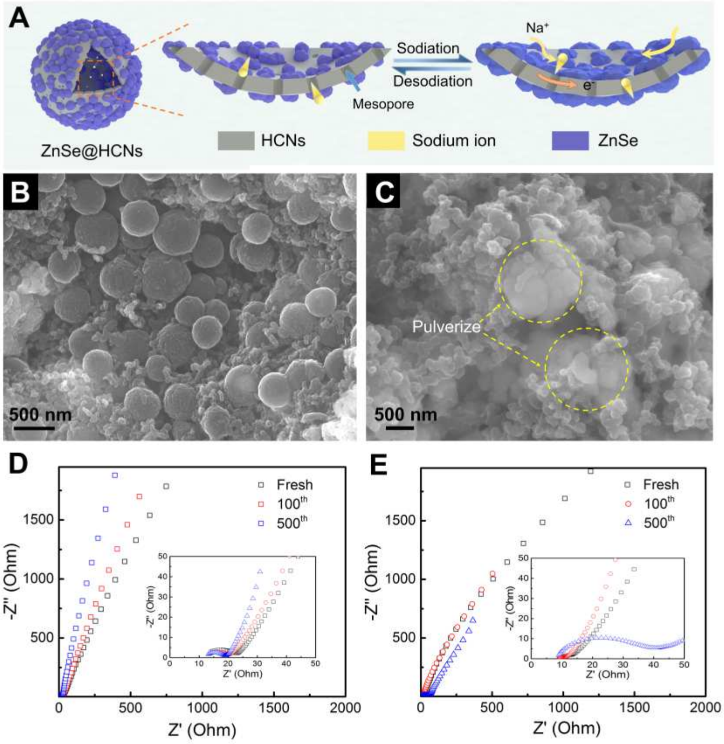

Figure 5. (A) Schematic illustration of the sodiation process of ZnSe@HCNs. (B, C) Ex-situ images and (D, E) Nyquist plots of (B, D) ZnSe@HCNs and (C, E) ZnSe MSs after 500 cycles.

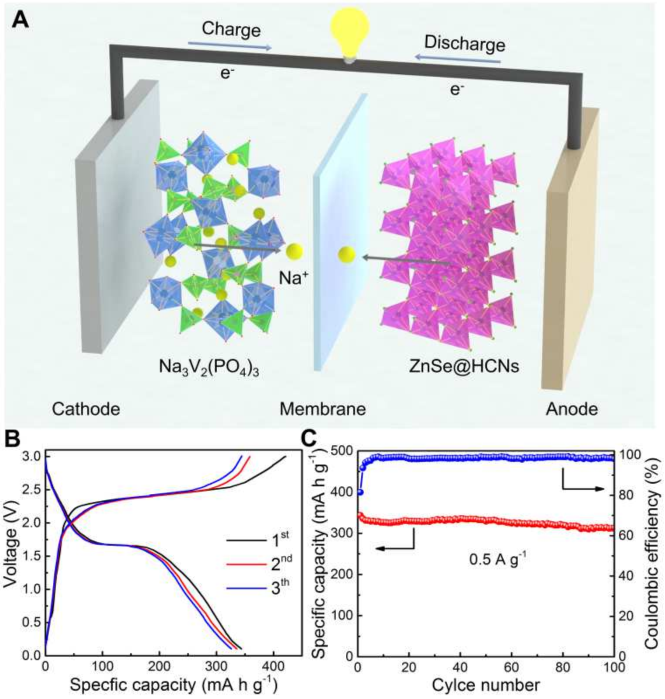

Figure 6. (A) Schematic illustration of the full sodium-ion battery with ZnSe@HCNs//NVP couple, (B) Charge and discharge profiles and (C) cycling performance and corresponding Coulombic efficiency of the full cells at 0.5 A g^{-1}.

Highlights

- ZnSe nanoparticles grow on both the inner walls and the outer surface of hollow carbon nanospheres (ZnSe@HCNs)
- The sodium storage mechanism of ZnSe@HCNs electrodes is a mixture of alloying and conversion reactions.
- A full cell constructed from the ZnSe@HCNs anode and $Na_3V_2(PO_4)_3$ cathode was demonstrated.
- ZnSe@HCNs exhibit long-cycle and high-rate sodium storage.
- The robust structure can accommodate the large volume and structural changes.

Shiyao Lu is currently a postgraduate in the Department of Chemistry of School of Science, Xi'an Jiaotong University under the supervision of Prof. Guoxin Gao. He received his B. S. degree (2016) in the same department. Currently, his research interests include alkali metal ion battery and nanostructured materials.

Tianxiang Zhu is currently a postgraduate in the Department of Chemistry of the School of Science, Xi'an Jiaotong University. He received his B. S. degree (2017) in Polymer Materials and Engineering from the School of Materials, Chang'an University. His research interest is the development of advanced lithium organic batteries.

Hu Wu received his B.S. degree in the school of Science, Xi'an Jiaotong University in 2018. He is now a Master Degree Candidate in Xi'an Jiaotong University. His research interest focuses on the synthesis and characterization of nanomaterials and electrochemical energy storage devices.

Yuankun Wang is currently pursuing his Ph.D. under the supervision of Prof. Shujiang Ding at Xi'an Jiaotong University, China. His research interests include rational design, fabrication and characterization of nanomaterials and their applications in energy storage and conversion.

Jiao Li received her Ph.D. degree in the School of Materials Science and Engineering from Xi'an Jiaotong University (XJTU) in 2017. Currently she is an experimental technician of transmission electron microscope in the Instrument Analysis Center of XJTU. Her research interest is focused on the microstructural characterization of materials.

Wei Wang is currently a postdoctoral researcher at Harvard University. He received his Ph.D. degree in Metallurgical Engineering in 2016 from University of Science and Technology Beijing, China. During 2014 and 2015, he studied at University of Cambridge as a joint Ph.D. student. His research interests include the design, synthesis and characterization of advanced energy materials for Li/Na/K/Al-ion batteries, solid-state electrolyte and catalysis.

Amor M. Abdelkader is associate professor of advanced materials at Bournemouth University and visiting academic at the University of Cambridge. He has received his PhD degree (2011) in Materials Science and Metallurgy from the University of Cambridge. His research activities cover a wide spectrum of materials topics ranging from newly discovered nanomaterials to traditional engineering materials such as alloys and ceramics, with strong focus on energy materials. He also have a strong interest in CO_2 sequestration.

Kai Xi is a research associate in the Cambridge Graphene Centre. He obtained his PhD degree in the Department of Materials Science and Metallurgy, University of Cambridge. His research focusses on materials engineering and physical chemistry for renewable energy conversion and storage, in particular lithium-sulphur (Li-S) batteries, lithium-ion batteries and solar cells. He was awarded the grand prize of the Dow Sustainability Innovation Student Challenge Award in 2013. His CamBattery team been awarded Technology Start Up of the Year by Cambridge University Entrepreneurs in 2012.

Yanguang Li received his B.S. in Chemistry from Fudan University, China in 2005; and obtained his Ph.D. in Chemistry from Ohio State University with Prof. Yiying Wu in 2010. He then moved to the Stanford University and completed a post-doctoral training with Prof. Hongjie Dai before taking the current faculty position in 2013. His research focuses on nanostructured functional materials for energy applications, particularly in the realm of electro-catalysis, advanced batteries and photo water splitting.

Guoxin Gao is an associate professor in the school of Science at Xi’an Jiaotong University. His main research interests are polymer gel electrolyte and nanostructured materials for electrochemical energy storage and conversion using supercapacitors, Li-ion, Na-ion and Li-S batteries.

Shujiang Ding is professor in the school of Science at Xi’an Jiaotong University. After being a postdoctoral fellow in Institute of Chemistry at Chinese Academy of Sciences (2007-2009), University of Central Florida (2009-2010) and Nanyang Technology University (2010-2011), he joined Xi’an Jiaotong University in 2011 and was promoted to full professor in 2014. His current research mainly focuses on electrochemical energy storage and conversion.

Professor Kumar has obtained his PhD from McMaster University, Canada and B.Tech (Hons) from IIT-Bombay in Materials Science & Metallurgy. He is the Head of Materials Chemistry Group and a Fellow of Trinity Hall in University of Cambridge, and a Fellow of the Institute of Materials, Mining and Metallurgy. He has published over 300 papers, 17 patents, 4 Chapters in Handbooks and 1 edited book (High energy density Li batteries, Wiley-VCH 2010, also translated in Chinese, 2013, 2nd Edition in 2019). He has supervised over 40 PhD students, 35 post-doctoral researchers, 20 visiting students and hosted 15 visiting professors.